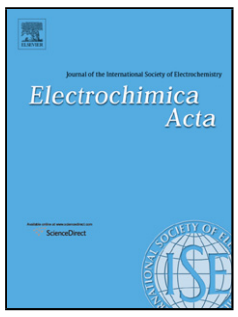

Title: *In operando* Synchrotron XRD/XAS Investigation of Sodium Insertion into the Prussian Blue Analogue Cathode Material $Na_{1.32}Mn[Fe(CN)_6]_{0.83}\cdot z\ H_2O$

Author: Jonas Sottmann Fabian L.M. Bernal Kirill V. Yusenko Matthias Herrmann Hermann Emerich David S. Wragg Serena Margadonna

PII: S0013-4686(16)30701-0
DOI: http://dx.doi.org/doi:10.1016/j.electacta.2016.03.131
Reference: EA 26961

To appear in: *Electrochimica Acta*

Received date: 2-2-2016
Revised date: 22-3-2016
Accepted date: 22-3-2016

Please cite this article as: Jonas Sottmann, Fabian L.M.Bernal, Kirill V.Yusenko, Matthias Herrmann, Hermann Emerich, David S.Wragg, Serena Margadonna, In operando Synchrotron XRD/XAS Investigation of Sodium Insertion into the Prussian Blue Analogue Cathode Material Na1.32Mn[Fe(CN)6]0.83*cdotz* H2O, Electrochimica Acta http://dx.doi.org/10.1016/j.electacta.2016.03.131

In operando Synchrotron XRD/XAS Investigation of Sodium Insertion into the Prussian Blue Analogue Cathode Material $Na_{1.32}Mn[Fe(CN)_6]_{0.83} \cdot z\ H_2O$

Jonas Sottmann,*[,a] Fabian L. M. Bernal,[a] Kirill V. Yusenko,[a,b] Matthias Herrmann,[a] Hermann Emerich,[c] David S. Wragg,*[,a] and Serena Margadonna[a,b]

[a] Chemistry Department and Centre for Material Science and Nanotechnology, University of Oslo, Norway.

[b] College of Engineering, Swansea University, Swansea SA2 8PP, UK.

[c] Swiss–Norwegian Beamlines, European Synchrotron, Grenoble, France.

* jonas.sottmann@smn.uio.no, david.wragg@smn.uio.

GRAPHICAL ABSTRACT

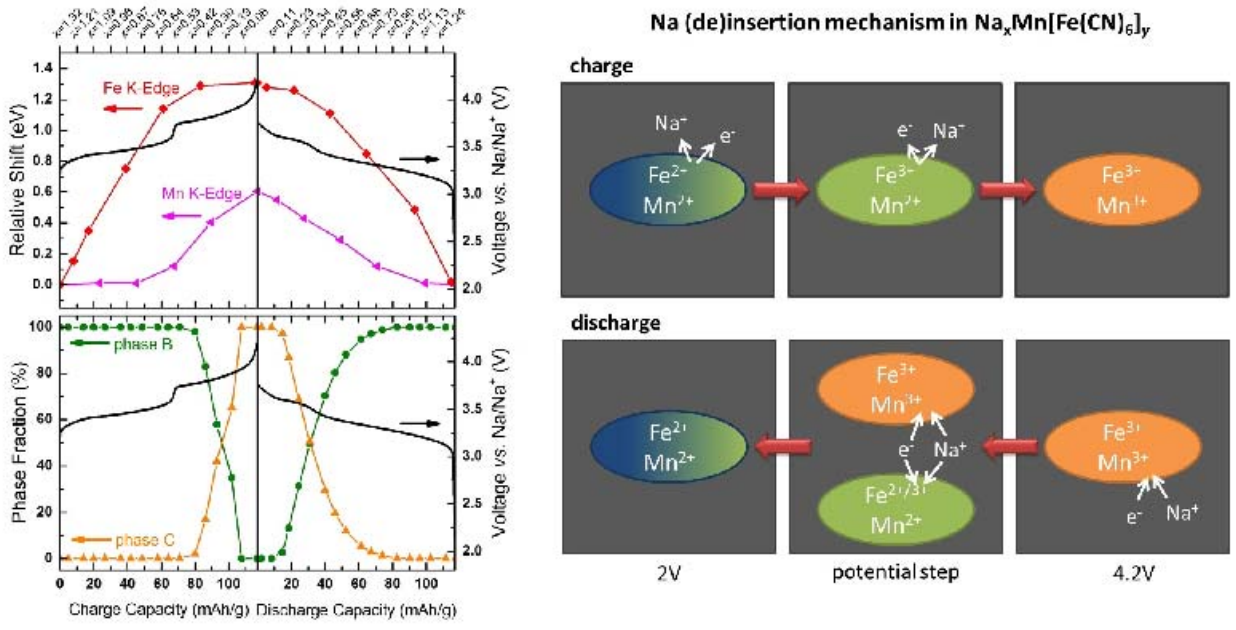

Abstract

Prussian Blue Analogues (PBAs) with general formula $Na_xM_A[M_B(CN)_6]_y \cdot z\ H_2O$ (M_A, M_B = transition metal) are promising low cost, high rate and high capacity cathodes for sodium ion battery (SIB) technology. Here, we have studied the PBA $Na_{1.32}Mn[Fe(CN)_6]_{0.83} \cdot z\ H_2O$ (z = 3.0 and 2.2) with varying structural modifications (monoclinic and cubic) using *in operando* quasi-simultaneous X-ray diffraction (XRD) and X-ray absorption spectroscopy (XAS). We observed a series of reversible structural phase transitions which accompany Na insertion/extraction during electrochemical cycling. The samples show pronounced differences in their galvanostatic charge and discharge profiles which could be linked to structural and electronic response. Different desodiation and sodiation mechanisms were identified. The

influence of $[Fe(CN)_6]$ vacancies and water content on the electrochemical performance was investigated.

Keywords

Battery; Sodium-ion; Hexacyanoferrates; Degradation; Water.

1. Introduction

Efficient energy storage is essential for the implementation of intermittent renewable energy sources into the electrical grid. Rechargeable battery technology can be used to balance electricity supply and demand. Today Lithium Ion Battery (LIB) technology dominates the portable devices and electric vehicle market. Unlike Li, Na is relatively cheap and readily available worldwide which might make it a viable option for large scale stationary storage. The realisation of the market potential of SIBs has boosted a large research effort into rechargeable, low-cost SIBs with reasonable energy density, high charge/discharge rate and durability[1, 2]. Ideal cathode materials for SIBs offer host-guest interactions in their 6-fold octahedral or prismatic coordination sites with negligible volume changes. Prominent examples are layered oxide materials and poly-anionic frameworks based on phosphates or sulphates [1-3].

Prussian blue analogues (PBAs), also referred to as metal hexacyanoferrates, with general formula, $Na_xM[Fe(CN)_6]_y \cdot zH_2O$ (M = transition metal, $x = 4y-2$, $y \leq 1$) have attracted substantial interest as promising cathode materials for SIBs. Generally, when M is Mn, Fe, Co or Ni, $M^{2+/3+}$ and $Fe^{2+/3+}$ reside on alternate corners of 8 sub cubes of corner-shared octahedra linked by linear $(C\equiv N)^-$ bridges in the face centred cubic (*fcc*) unit cell (Fm-3m, $Z = 4$). The low-spin (LS) $Fe^{2+/3+}$ bonds with C atoms while the high-spin (HS) $M^{2+/3+}$ bonds with N atoms. Coordinating water resides in the randomly distributed $[Fe(CN)_6]$ vacancies (6 H_2O molecules per vacancy), while zeolitic water and Na-ions can be found in the nanosized voids of the

framework structure. The Na-ions diffuse across the faces of the sub cubes formed by the $(C\equiv N)^-$ ligands which compared to O^{2-} ions interact less with Na^+ [4].

High specific capacities can be achieved in these compounds due to a potential two-electron per formula unit redox reaction. Reversible Na insertion/extraction into PBA has been demonstrated for M = Mn, Fe, Co, Ni, Cu and Zn [4]. For M = Fe promising high rate performance and high specific capacity of up to 170 mAh/g with good cycling stability were obtained by controlling water content, number of vacancies and crystallite size [5-7]. For M = Mn similar high rate capability, but lower capacity were found [8-10]. Wang *et al.*[9] reported 134 mAh/g initial discharge capacity for a distorted PBA structure with composition $Na_{1.72}Mn[Fe(CN)_6]_{0.99}\cdot 2.3H_2O$. After 30 cycles 90 % of the initial discharge capacity was retained. For a non-distorted PBA cubic structure with composition $Na_{1.40}Mn[Fe(CN)_6]_{0.97}\cdot 3.3H_2O$ they observed lower initial discharge capacity (123 mAh/g) but improved capacity retention (96 % after 30 cycles). The capacity degradation was therefore ascribed to the expected phase transitions between distorted and cubic structure when Na is extracted from and inserted into the structure during the electrochemical cycles. Starting from non-distorted manganese hexacyanoferrate thin films depending on the initial composition (y = 0.83, 0.87 and 0.93) Moritomo *et al.* observed different structural changes against Li content [11]. For $Na_{1.32}Mn[Fe(CN)_6]_{0.83}\cdot 3.5H_2O$ they report a single cubic phase with different lattice parameters for different Na content. The discharge profiles of Na and Li analogues (y = 0.83) show different features (two well separated flat plateaus for Li and only slightly separated sloped plateaus for Na) and thus different sodiation and lithiation mechanisms might be expected.

A fundamental understanding of extraction/insertion processes (single phase vs. two-phase), structural stability and voltage-composition profiles is pivotal for optimisation of electrode

materials. In addition to X-Ray Diffraction (XRD) which probes the long range order, X-ray Absorption Spectroscopy (XAS) can be used to determine changes in oxidation state and fine structural details such as C≡N bond length and M_A-C≡N-M_B orientation in metal hexacyanoferrates [11-14]. *In operando* quasi-simultaneous powder XRD and XAS where the structural and electronic response of the electrodes is constantly monitored during continuous cycling are therefore powerful techniques for understanding a materials electrochemical performance.

Here we report the first *in operando* quasi-simultaneous XRD and XAS investigation of the PBAs $Na_{1.32}Mn[Fe(CN)_6]_{0.83} \cdot z\ H_2O$ (z = 3.0 and 2.2) with varying structural modifications (distorted and non-distorted PBA structures similar to those observed by Wang *et al.*[9]) as cathode material for SIBs. Contrary to the previous findings [11] we observed a series of reversible structural phase transitions that are clearly linked to the galvanostatic charge and discharge profiles. The influence of the different water content on the electrochemical performance was also studied. Our data give a deeper insight into the possible reasons for capacity degradation in this family of materials.

2. Experimental

2.1 Material Synthesis and Characterization

Both samples were prepared by a simple precipitation method: First, 14 g NaCl (Sigma Aldrich) were dissolved in 100 ml of 0.1 M $Na_4Fe(CN)_6 \cdot 10\ H_2O$ (Alfa Aesar) aqueous solution. Then 50 ml of 0.2 M $Mn(NO_3)_2 \cdot 4H_2O$ (Sigma Aldrich) aqueous solution was added dropwise to the $Na_4Fe(CN)_6$ and NaCl solution under continuous stirring. The final solution was left to age at room temperature overnight. Further, filtering and washing with deionized water was carried out. The sample was then divided into two batches and dried for 6 hours: the first batch was dried at 60 °C (sample **I**), and the second at 120 °C (sample **II**).

Powder X-ray diffraction measurements with Cu Kα1 radiation were performed in transmission mode on a Bruker D8 with samples sealed in 0.5 mm diameter thin-walled glass capillaries (Hilgenberg GmbH). Diffraction profiles collected before and after drying are shown in Figure S1. Energy-Dispersive X-ray spectroscopy (EDX) was carried out at 15.0 kV on a Hitachi SU8200. It revealed a chemical composition of Na, Fe, Mn, C, N, O elements in the absence of any discernible Cl element. The molar ratios of Na, Mn and Fe were measured by Microwave Plasma-Atomic Emission Spectrometry (MP-AES 4100, Agilent Technologies) analysis and normalized to the Mn content. A composition of $Na_{1.32}Mn[Fe(CN)_6]_{0.83}$ was obtained for both samples. Thermogravimetric analysis (STA 1500, Scinco Co. Ltd) was conducted in an open alumina crucible in air from room temperature to 400 °C at a heating rate of 10 °C/min (Figure S2). Water contents of 17 wt% and 13 wt% were obtained for samples **I** and **II**, respectively. Combining MP-AES and STA results gives a stoichiometry of $Na_{1.32}Mn[Fe(CN)_6]_{0.83} \cdot z\ H_2O$ with $z = 3.0$ and $z = 2.2$ for samples **I** and **II**, respectively. Sample **II** tends to absorb water with time and the samples were therefore stored in an Ar-filled glovebox (M. Braun). Magnetic susceptibility (χ_M) measurements were carried out in the temperature range 5 K to 300 K under a magnetic field of 1 T using a Magnetic Property Measurement System (MPMS, Quantum Design). The magnetic susceptibility of sample **I** was measured representatively for both samples. Paramagnetic behaviour and no phase transitions were observed over the whole temperature range (Figure S3). The as determined effective magnetic moment (μ_{eff}) of $5.6\mu_B$ per formula unit is close to the theoretical value for a purely HS Mn^{2+} ($S = 5/2$) and LS Fe^{2+} ($S = 0$) configuration ($\mu_{eff} = 5.9\mu_B$).

2.2 Electrochemical Measurements

For the electrochemical characterization coin cells (2032) were assembled in an Ar-filled glove box with H_2O and O_2 levels less than 0.1 ppm (M. Braun). The working electrode composition

was 70 wt% of sample **I** or sample **II** as active material, 20 wt% of conductive carbon black (Timcal Super P) and 10 wt% polytetrafluoroethylene (PTFE) binder. The mixture was rolled into a thin film with a mass loading of active material of about 5 mg/cm^2. The working electrode was separated from the Na metal disk as counter electrode by electrolyte soaked glass fibre. The electrolyte used was a 1 M solution of $NaClO_4$ in ethylene carbonate/diethyl carbonate (1:1 in vol.) solution. The cells were left at open circuit for at least 3 h to make sure the electrolyte was fully soaked into the electrode before galvanostatic cycling between 2 V and 4.2 V at a current rate of C/10 (1C ≡ 120 mA/g).

2.3 *In operando* Synchrotron XRD and XAS measurements

In operando quasi-simultaneous powder X-ray diffraction and absorption measurements were performed at the Swiss-Norwegian Beam Lines (SNBL), BM01B, at the European Synchrotron (ESRF). Diffraction profiles were collected using the Dexela 2923 CMOS 2D detector. The wavelength (λ = 0.50497 Å) was calibrated by means of a Si NIST standard. For data reduction the FIT2D software [15] was used. Spotlike reflections from the Na metal were masked prior to integration. All profile fittings and Rietveld refinements were performed using TOPAS V4.2 (Bruker AXS). For each individual powder pattern zero-shift, background (13 term Chebychev polynomial), cell parameters, peak-profile parameters for the individual phases, as well as their scale factor, were refined in parallel for all powder patterns in each dataset. Reflections from the textured Al foil were fitted with a structureless phase with the lattice parameter and space group of Al metal (a = 4.05 Å, *Fm*-3*m*) and from the PTFE with a peak at 5.88°. For two-dimensional detectors the counting statistics of the diffraction pattern cannot be estimated by the square root of the counts as the number of pixels integrated under the diffraction rings is not constant throughout the angular range of the diffraction pattern. The refinement software will, however, assume the square root of the counts as standard deviation if not otherwise

specified which results in high *Rexp* values. X-ray Absorption Near Edge Spectroscopy (XANES) were collected at the Mn K-edge (from 6460 to 6750 eV) and at the Fe K-edge (from 7050 to 7280 eV) in transmission mode using a Si-(1 1 1) channel-cut type monochromator. The second crystal was detuned at about 70 % to reduce higher harmonics. The XANES data were analysed using ATHENA [16] for absorption edge determination and spectrum normalization to an edge jump of unity. The absorption edge position was determined as the maximum of the first derivative of the spectrum as exemplarily shown in Figure S7. The relative shift in absorption energy was calculated with respect to the pristine material. The energy resolution in this setup is 1.4×10^{-4} eV and the standard deviation observed in four separate measurements of the absorption edge at the same charge state was 0.04 eV. The electrochemical cycling was performed in Swagelok type electrochemical cells with Kapton windows which are available at SNBL. The battery assembly was kept identical to the coin cells. The first galvanostatic cycle was followed *in operando* at a current rate of C/10 which means that each charge/discharge took approximately 10 h. Due to the high rate capabilities of manganese hexacyanoferrates [9, 10] close to equilibrium conditions and negligible interference with the absorption energies are assumed at a C/10 rate. XRD and XANES (Fe and Mn K-edges) data collection (7 min per XRD scan and 3 min per XANES scan) were performed in sequence on the same cell. No beam damage to electrode or electrolyte components was observed during repeated X-ray exposure over the duration of the experiment.

2.4 *Ex situ* XRD studies

Ex situ synchrotron XRD profiles of the pristine active materials were collected separately. For this purpose, samples **I** and **II** were sealed under Ar in 0.3 mm diameter thin-walled glass capillaries (Hilgenberg GmbH).

Ex situ home lab XRD data (Bruker D8) were collected on both samples cycled five times in a reduced potential range (2 V to 3.8 V) and the full potential range (2 V to 4.2 V), and compared to pristine materials recovered from cells that were left at open circuit voltage while the other cells were cycled. All coin cells were disassembled in an Ar-filled glovebox (M. Braun). The recovered working electrodes were sealed under Ar in 0.5 mm diameter thin-walled glass capillaries (Hilgenberg GmbH).

3. Results

3.1 Electrochemistry

Figure 1 shows the results of the electrochemical measurements. The redox reaction at low and high potential correspond to the LS Fe^{2+}/Fe^{3+} and the HS Mn^{2+}/Mn^{3+} couples, respectively [8, 11]. In the first charge (Figure 1b), a pronounced step from low to high potential plateau is observed at identical capacity (70 mAh/g) for samples **I** and **II**. However, in sample **I** the oxidations take place at higher potential (3.49 V and 3.91 V) compared to sample **II** (3.46 V and 3.83 V). The difference is not as pronounced for the Fe^{2+}/Fe^{3+} as it is for the Mn^{2+}/Mn^{3+} redox reaction. Samples **I** and **II** have first charge (discharge) capacities of110 mAh/g (107 mAh/g) and 117 mAh/g (117 mAh/g) in the synchrotron electrochemical cell, which are comparable to their theoretical capacities of 112 mAh/g and 118 mAh/g. During discharge, the higher potential plateau is shortened while the lower is extended and the step between the two plateaus is drastically smoothed. The step is observed at 23 mAh/g and 34 mAh/g discharge capacity for samples **I** and **II**, respectively. In sample **I** reduction potentials were observed at lower potentials (3.29 V and 3.53 V) compared to sample **II** (3.31 V and 3.61 V). Overpotential is observed in both samples but is higher for sample **I** (Figures S4a and S4b). With increasing cycle number the pronounced step between the redox potentials during charge is smoothed and becomes more similar to the discharge profile in both samples (Figures 1c and 1d). However,

plotting voltage profile versus normalized specific capacity reveals that this is due to lowering of the oxidation energy of the $Mn^{2+/}Mn^{3+}$ couple by 0.08 V for sample **I** and 0.06 V for sample **II**, while the Fe oxidation plateau remains unchanged in energy and slope with increasing cycle number (Figures S5a and S5b). Interestingly, the reduction energies decrease over almost the entire width of the voltage profile versus normalized specific capacity during the series of discharge steps in both samples (Figures S5c and S5d). Sample **I** shows pronounced sloping in the higher potential plateau. Furthermore, the drastic change in slope expected at the end of each plateau is not observed. This might indicate that the oxidation of Mn^{2+} in sample **I** cannot be completed before the cut-off potential is reached. The shoulder in the differential capacity (dQ/dV) curves of sample **I** after the first cycle at voltages above 3.8 V (Figure S4c) further indicates that irreversible side reactions are taking place. Sample **I** shows pronounced capacity degradation during the first cycles. Only 83 % (87 mAh/g) of its first discharge capacity are retained after 5 cycles (Figure 1a). The capacity degradation is strongest in the Mn^{2+}/Mn^{3+} plateau as can be seen from the shift in relative capacity contribution of each redox couple in Figure S5a. The step between Fe and Mn oxidation plateau moves from 58 % to 63 % normalized specific capacity which indicates that the contribution of the Mn^{2+}/Mn^{3+} couple to the total capacity is reduced by 5% over the first 5 cycles. Irreversible side reactions above 3.8 V seem to be less pronounced for sample **II** (Figure S4d). For sample **II** the discharge capacity is relatively stable and close to its theoretical value. After 5 cycles a discharge capacity of 115 mAh/g was found (Figure 1a). The capacity contribution of both redox couples remains almost constant during the first cycles. The ratio Fe and Mn oxidation plateau stays at about 58 % (Figure S5b). In both materials the stability of the $Fe^{2+/3+}$ redox couple in the PBA structure is further confirmed by negligible capacity degradation over at least 30 cycles if the potential window is limited to the lower potential plateau, from 2 V to 3.6 V (Figure S6). Both samples show approximately constant Coulombic efficiency at about 80 % for sample **I** and 90 % for

sample **II** (inset Figure 1a). In sample **I** we observe lower voltage and Coulombic efficiency as well as pronounced capacity degradation compared to sample **II**.

3.2 Structure of the pristine materials – cubic and monoclinic distorted PBA phases

The *fcc* structure of PBAs was described in the introduction. Figure S1 shows the XRD profiles of the pristine materials. Both materials are single phase. The XRD pattern of sample **II** can be indexed with the *fcc* PBA structure. In the XRD pattern of sample **I** the (1 1 1), (0 2 2) and (0 4 2) Bragg reflections of the *fcc* PBA structure are split. Distorted PBA structures have been reported in the literature [10, 17-20]. For $Na_{1.32}Mn[Fe(CN)_6]_{0.83}\cdot 3.6H_2O$ a rhombohedral distortion (R-3m, Z = 12) was found after cooling the initially *fcc* structure below 280 K [20]. For their structural refinements of the rhombohedral structure Moritomo *et al.* constrained several bond distances and bond angles to keep the shape of the cyano-bridged framework of the *fcc* structure. It was argued that the symmetry change is caused by a cooperative displacement of the Na-ions via dipole-dipole interactions along the cubic [1 1 1] direction. For $Na_2Mn[Mn(CN)_6]\cdot 2H_2O$ Kareis *et al.* observed a monoclinic structure ($P2_1/n$, Z = 2) that was stable from room temperature down to 15 K [17]. Here the average Mn-C-N bond angles are significantly distorted away from linearity to minimize void space. Song *et al.* also found this space group for $Na_2Mn[Fe(CN)_6]\cdot 1.9H_2O$ [10]. The monoclinic distortion was assigned to a cooperative displacement of $(NaOH_2)^+$ groups in alternating cubic [1 1 1] and [1 -1 1] directions. Rietveld refinements using these models do not fit the experimental data perfectly, indicating that there are still deficiencies in the models, despite the fact that all peaks are indexed by the unit cells. This makes it difficult to use the Rietveld fits to choose between the possible structure types.

In order to obtain the best possible fit and distinguish between the rhombohedral and monoclinic forms structureless Pawley refinement was used. Sample **I** gave a better fit for the

monoclinic (R_{wp} = 1.67 %) than for the rhombohedral unit cell (R_{wp} = 2.93 %). The results of the Pawley refinements, lattice and R-factors are presented in Figure S8. The rhombohedral model is furthermore questionable because of a bad fit of the split cubic $[0\ 2\ 2]_c$ reflections and a larger and positive zero shift compared to sample **II**. The monoclinic model fits all reflections of the collected XRD profile and the zero shift is in good agreement with sample **II**.

Initial Rietveld refinements were performed on the pristine samples **I** and **II** to provide a starting point for parallel Rietveld refinement of the electrochemical cycling data.

In view of the Pawley refinement results we proceeded with a Rietveld refinement of sample **I** in the monoclinic model [10, 17] where Fe replaces the C-bound Mn and additional zeolitic water sites (4*e*) are found close to each face of the cubic subunits. Isotropic temperature parameters were fixed to those obtained for sample **II**. Atomic positions were refined with restraints on distances and angles. The occupancies were found to be close to the results from thermogravimetric and elemental analysis. The results of the Rietveld refinement are shown in Table 1 and Figure 2a. The monoclinic phase gives a good description for sample **I** and is hereafter referred to as phase **A**. Sample **II** has the *fcc* PBA structure. The structural model suggested by Moritomo *et al.*[20] with Na in tetrahedral (32*f*) and zeolitic water in octahedral sites (48*g*) gave the best fit. The results of the Rietveld refinement are shown in Table 1 and Figure S9. The cubic structure will hereafter be referred to as phase **B** and if fully desodiated as phase **C**. A representation of each phase is shown in Figure 2b.

3.3 *In operando* synchrotron quasi-simultaneous XAS and XRD measurements

Figures 3a-b show normalised Mn and Fe K-edge XANES spectra that were collected during the first discharge (sodiation) in sample **I**. Signatures for both Mn^{3+} and Mn^{2+} are found in the XANES spectrum of the desodiated sample (x = 0.00). During discharge the Mn^{3+} ions are reduced first and the average oxidation state of Mn changes towards 2+ (Figure 3a). Changes

are more pronounced for discharge capacities below 48 mAh/g ($x < 0.59$). The oxidation state of Fe remains constant until the potential step between high and low potential plateau is reached at about 23 mAh/g discharge capacity ($x = 0.29$). In the low potential plateau the average Fe oxidation state reduces from 3+ to 2+ with increasing Na content (Figure 3b). These findings are in good agreement with the literature reports on the Li/Na analogues [11]. However, the compositional range (x) over which the Mn oxidation state changes during discharge deviates. In this work the XAS analysis was limited to following oxidation state changes, i. e. the relative shift in absorption edge positions. Further insight to the element specific local environment could be obtained by studying the pre-edge features and extended X-ray absorption fine structure (EXAFS) [12, 13, 21].

Figures 4a-b and 5a-b show the relative shift in Fe and Mn absorption edge for samples **I** and **II**, respectively, and compares them to their respective voltage profiles during the first electrochemical cycle. The initial Fe and Mn absorption edge positions are identical for the pristine samples **I** and **II**. During charge the Fe K-edge shifts to higher energies in the lower potential plateau, it remains unchanged in the high potential plateau and moves back to its initial value after the lower potential plateau is reached during discharge in both samples. Between sodiated and desodiated state a similar reversible relative shift in Fe K-edge of about 1.3 eV was observed for samples **I** and **II** (Figures 4a and 5a). During charge the position of the Mn K-edge remains unchanged in the lower potential plateau but starts to shift to higher energies as soon as the higher potential plateau is reached for both samples. Between the sodiated and desodiated states a reversible relative shift in Mn K-edge of about 0.3 eV and 0.6 eV was found for samples **I** and **II**, respectively (Figures 4b and 5b). Even though a calibration curve of the formal oxidation state *vs.* XANES threshold is not provided, the larger relative shifts of the Fe K-edges compared to the Mn K-edges suggest different redox-activities of both metals. The relative change in Mn absorption edge position is much more pronounced for

sample **II** which means that more Mn^{3+} is formed and more Na extracted from the PBA. While all Mn oxidation during charging took place in the higher potential plateau, only about half of the total reverse shift in absorption edge position is completed in this plateau during discharge. Thus both Mn and Fe reduction are found in the lower potential plateau during discharge.

Our *in operando* synchrotron XRD reveals a series of reversible phase transitions between the three distinct phases of $Na_xMn[Fe(CN)_6]_{0.83}$ during galvanostatic charge and discharge. We used Rietveld quantitative analysis to study the phases present at different stages of electrochemical cycling. All atom positions, occupancies and thermal parameters were fixed to the values from the initial refinements of phases **A** and **B**.

Figures 3c-d show selected Bragg reflections of the XRD profiles which illustrate the phase transitions during discharge in sample **I**. After the first charge (desodiation) the diffraction profiles clearly show the presence of two distinct phases, namely phase **B** and phase **C** with smaller lattice constants $a = 10.3490(2)$ Å. Rietveld refinements confirmed that in the latter the Na content is negligible. During discharge, the intensity of phase **C** decreases while it increases for phase **B** which indicates that phase **C** is gradually transformed to phase **B** (Figure 3c). At sufficient Na content (70 mAh/g discharge capacity, $x = 0.86$) the *fcc* reflections start to split. This is characteristic of the transition of phase **B** to phase **A** as shown Figure 3d. With increasing Na content the splitting of the reflections gets more pronounced. For the Rietveld refinements we can first distinguish between phase **B** and **A** when the splitting of the reflections is sufficiently large. Even if the peaks start to split at 70 mAh/g discharge capacity ($x = 0.86$) the best fit is obtained for phase **B** with $a = 10.5745(2)$ Å. At 76 mAh/g discharge capacity ($x = 0.94$), however, the structure is best fitted in phase **A** with normalised lattice parameters close to the those of phase **B** before the transition ($a_{c,a} = a = 10.569(1)$ Å, $a_{c,b} = \sqrt{2}\, b = 10.580(1)$ Å, $a_{c,c} = \sqrt{2}\, c = 10.558(1)$ Å, $\beta = 91.39(1)°$). With increasing Na content the monoclinic distortion

is increased and lattice parameter and angle become less metrically cubic as can be seen in Figure S10. A similar phase transformation (between **B** and **C**) has been observed for the Li analogues (y = 0.87) but no structural phase transformations were reported for the Li/Na analogues (y = 0.83) with varying x [11].

Figures 4c-d and 5c-d show the phase fractions of the three distinct phases and their volume changes during the first electrochemical cycle in samples **I** and **II**, respectively. In the pristine cell with sample **I** we observe phase **A** with a volume of 292.9 $Å^3$ per unit formula. During desodiation the distortion of the monoclinic PBA is smoothly reduced and as a result the volume contraction of phase **A** is released. The cyanide framework returns to linearity when Na is extracted. At $x \approx 0.9$ (27 mAh/g charge and 76 mAh/g discharge capacity) and 3.0 H_2O per formula unit the structure can be fully described as phase **B**. The pristine cell with sample **II** (1.32 Na and 2.2 H_2O per formula unit) contains only phase **B** in the lower potential plateau. Desodiation of phase **B** also leads to volume relaxation until it reaches a maximum of 298.2 $Å^3$ (295.8 $Å^3$) per formula unit for sample **I** (**II**). At the step to the higher potential plateau formation of phase **C** is detected. In this plateau phase **B** is gradually transformed into phase **C**. During this process the volume of phase **B** remains close to its maximum value while the volume of phase **C** decreases from 280.3 $Å^3$ to 277.1 $Å^3$ (281.2 $Å^3$ to 274.6 $Å^3$) for sample **I** (**II**). While the volume difference for phases **A** and **B** in the lower potential plateau is relatively small it is noticeable for phases **B** and **C** in the higher potential plateau. The pronounced difference in volume between phases **B** and **C** can indeed be explained by the pronounced difference in ionic radii for HS Mn^{3+} (0.970 Å) and HS Mn^{2+} (0.785 Å) while it is insignificant for LS Fe^{3+} (0.69 Å) and LS Fe^{2+} (0.75 Å) in 6 coordinate octahedral environment[22]. At the end of the first charge only about 90% of phase **B** was transformed to phase **C** for sample **I** while the transformation was complete for sample **II**. The complete transformation and the bigger change in volume of phase **C** for sample **II** are a further confirmation that more Mn^{2+} is

formed in sample **II** compared to sample **I** at the end of charge. During discharge phase **C** transforms back to phase **B** in both samples. The volume of phase **B** remains constant in the higher potential plateau while the volume of phase **C** reversibly increases towards the step to the lower potential plateau which is observed at 23 mAh/g (34 mAh/g) discharge capacity for sample **I** (**II**). At the step, phase **C** still exists and phases **C** and **B** are present in equal amounts. In contrast to the charge process phase **C** is also found in the lower potential plateau during discharge. After the step in potential the phase transformation from phase **C** to **B** continues as the trend in phase fractions indicates. The volume of phase **C** does not increase above its initial volume of formation and the volume of phase **B** decreases which indicates Na insertion into this phase. The transition to phase **B** is completed at 54 mAh/g (67 mAh/g) discharge capacity for sample **I** (**II**) which corresponds to about 30 mAh/g after the step for both samples. The volume of phase **B** is continuously compressed with Na insertion. For sample **I** phase **B** transforms back to phase **A** at 70 mAh/g discharge capacity. The volume compression continues also in phase **A** for sample **I** during further sodiation. At the end of the first cycle samples **I** and **II** are found in the form of phase **A** and **B**, respectively, with lattice parameters in good agreement with those of the pristine samples. The phase transitions were thus fully reversible during the first electrochemical cycle, however, differences in the phase evolution during galvanostatic charge and discharge were observed.

3.4 *Ex situ* XRD studies after five cycles

The *ex situ* XRD profiles of the materials cycled over the full potential range are shown in Figure 6. They reveal the presence of new reflections from $NaMnCl_3$ (PDF-number 01-070-1322) which are much more pronounced for sample **I** but also present in sample **II**. The *ex situ* XRD profiles of the cells cycled in the reduced potential range (up to 3.8 V) are almost identical to those of the pristine samples (Figure S11). These observations indicate that the structural

transformations identified by *in operando* measurements take place reversibly below 3.8 V, while the irreversible reactions leading to the formation of $NaMnCl_3$ occur at voltages above 3.8 V. The amount of $NaMnCl_3$ is likely to increase with cycle number as a phase fraction sufficient for detection by XRD is first observed after several cycles. The formation of $NaMnCl_3$ further seems to be favoured by presence of water (z = 3.0 and z = 2.2 for samples **I** and **II**, respectively).

4. Discussion

4.1 Sodiation and desodiation mechanisms in $Na_xMn[(FeCN)_6]_y$

Both materials show a series of reversible phase transitions. Differences in charge and discharge mechanisms were observed in electrochemical and structural data for both samples. The lower and higher potential plateaus are clearly separated during charge, while the higher potential plateau is shortened and the potential difference between the plateaus is much smaller during galvanostatic discharge. Also the discharge profile is more sloped than the charge profile. Due to the higher content of guest atoms (Na and water), sample **I** initially adopts a monoclinic structure (phase **A**). During charge Na is removed and the structure relaxes to the PBA *fcc* structure (phase **B**) in the lower potential plateau. In sample **II** phase **B** is present initially due to the lower water content. The average Fe oxidation state changes from 2+ to 3+ during desodiation in the lower potential plateau. Formation of phase **C** (from phase **B**) is associated with partial oxidation of Mn^{2+} to Mn^{3+} upon further desodiation in the higher potential plateau. At the end of the charge this transition is completed for sample **II** but not for sample **I**. During discharge, however, phase **C** is continuously transformed to phase **B** by taking up Na and reducing Mn^{3+} to Mn^{2+} in the lower potential plateau. At the step between higher and lower potential plateaus the phase fraction of phase **B** is sufficient to allow for detectable Na insertion by reduction of Fe^{3+} which is confirmed by the volume compression of phase **B**

and the XANES analysis. Both phases are available for Na insertion and both Fe^{3+} and Mn^{3+} can be reduced simultaneously. The reduction potential is thus an average of the overall Mn^{3+} and Fe^{3+} reduction potentials in the region of coexistence of phase **C** and phase **B**. During the whole charge process only one phase at the time is available for Na extraction (phase **A** or phase **B**) while during discharge Na-ions can be inserted in phase **C** and phase **B** simultaneously. These observations can explain the shortening of the higher potential plateau, the smoothing of the potential step and the change in slope during discharge compared to the charge process. An illustration of the different sodiation and desodiation mechanisms is presented in Figure S12.

4.2 Influence of the water content in $Na_xMn[(FeCN)_6]_y \cdot z\ H_2O$ and other reasons for capacity degradation

Samples **I** and **II** originate from the same precipitation synthesis but were exposed to different drying conditions resulting in a final formula of $Na_{1.32}Mn[Fe(CN)_6]_{0.83} \cdot z\ H_2O$ with $z = 3.0$ and $z = 2.2$, respectively. The coordinating and zeolitic water contents thus have a major impact on the cycling performance. In sample **I** we observe lower voltage and Coulombic efficiency as well as pronounced capacity degradation compared to sample **II**. The higher zeolitic water content in sample **I** might reduce the diffusivity of Na^+ along the 3D tunnel pathways in the PBA framework structure, building up larger overpotential and thus lower voltage efficiency. The increased overpotential might also be one reason why sample **I** does not achieve the same average Mn oxidation as sample **II** and does not fully desodiate (formation of phase **C**) before the cut-off potential is reached. At the same time our *ex situ* studies showed that an irreversible side reaction occurs above 3.8 V which is favoured by higher water contents. This irreversible side reaction reduces the Coloumbic efficiency of the material and leads to loss of Mn in the form of $NaMnCl_3$ and pronounced capacity degradation. The capacity degradation in sample **I**

cannot be ascribed to the monoclinic to cubic phase transition because of the high cycling stability in the $Fe^{2+/3+}$ plateau in which this transition takes place. This is further confirmed by the reversibility of the structural changes observed by our *in operando* and *ex situ* measurements. Low Coulombic efficiency could also be due to removal of water from the structure during cycling as assumed in the literature [4, 23]. Electrochemical removal of interstitial water was confirmed for $Na_2Mn[(FeCN)_6]\cdot 1.9H_2O$ [10]. Here this would only fit with the reversible structural changes if the water were replaced by Na during discharge. Neutron diffraction data would be necessary to gain further insight.

The exact formation mechanism of $NaMnCl_3$ is subject for future investigations. As measured by EDX no Cl is found in the pristine samples. The Cl must therefore originate from the ClO_4^- ions in the electrolyte. The need to reinvestigate the reduction process of the perchlorate anion (normally assumed to be very stable) was outlined in a recent review on the electrochemical/electrocatalytic stability of ClO_4^- at any electrode used in aqueous media [24]. A high potential (> 3.8 V) is considered necessary to drive the decomposition of the ClO_4^- ions. Furthermore, our data suggest that higher zeolitic water concentrations promote the process of $NaMnCl_3$ formation. Manganese dissolution might be favoured by the presence of $[Fe(CN)_6]$ vacancies substituted by water molecules when compared to vacancy free manganese hexacyanoferrates [9, 10] where no Mn dissolution and/or no residual formation were found. Using $NaPF_6$ instead of $NaClO_4$ as electrolyte salt does not improve cycling stability. A similar degradation mechanism might be assumed for both salts. Ageing mechanisms in LIBs involving Mn dissolution and electrolyte decomposition as reported in Ref. [25] might provide guidance in understanding the processes involved.

The reason for the capacity degradation in the $[Fe(CN)_6]$ vacancy free sodium manganese hexacyanoferrates reported in Ref. [9] can neither be found in the phase transition from

distorted to cubic PBA nor Mn disintegration but might be due to large volume changes during cycling. The trend in volume change is very similar for both samples. Sample **I** has on average a slightly larger volume (about 2 $Å^3$ for all phases) than sample **II**. The volume change from the pristine samples to the partly desodiated phase **B** at the end of the lower plateau is relatively low (about 2 %). However, the phase transition from phase **B** to **C** in the higher potential plateau is accompanied by a large volume change for insertion materials of up to about 8 % which might add a lot of stress on the grain boundaries of manganese hexacyanoferrate framework structures. Phase transitions together with large volume changes (above 4%) are often associated with damage to the structure and particle-to-particle contacts which reduces electrochemical cyclability [25-28].

5. Conclusions

Our investigation clearly demonstrates that synthetic conditions influencing the amount of $[Fe(CN)_6]$ vacancies and water content are critical for the performance of PBAs in a battery. For $Na_{1.32}Mn[Fe(CN)_6]_{0.83} \cdot zH_2O$ we found strong correlation between not only changes in the transition metals oxidation states but also structural response during cycling and electrochemical performance of the battery. Pronounced differences in the galvanostatic cycle could be linked to the structural changes which follow necessarily different paths during charge and discharge. With repeated cycling the active material loses Mn in the form of $NaMnCl_3$ which causes capacity degradation. Loss of capacity appears to be promoted by both coordinating water in $[Fe(CN)_6]$ vacancies and higher zeolitic water content in the pristine material. Relatively large volume changes between the sodiated and desodiated phases may also contribute to capacity degradation.

Acknowledgements

The authors thank Bjørn-Tore Lønstad Bleken and Sharmala Aravinthan (University of Oslo, Oslo, Norway) for contributions on ICP and TGA. The authors thank Sébastian Sallard (PSI, Villigen, Switzerland) and Wouter van Beek (SNBL, Grenoble, France) for valuable discussions. This work was supported by the synchrotron and neutron travel grant (Research Council of Norway, No. 216625). We acknowledge use of the Norwegian national infrastructure for X-ray diffraction and Scattering (RECX).

References

[1] M.D. Slater, D. Kim, E. Lee, C.S. Johnson, Sodium-Ion Batteries, Adv. Funct. Mater., 23 (2013) 947-958.
[2] V. Palomares, P. Serras, I. Villaluenga, K.B. Hueso, J. Carretero-Gonzalez, T. Rojo, Na-ion batteries, recent advances and present challenges to become low cost energy storage systems, Energy Environ. Sci., 5 (2012) 5884-5901.
[3] H. Pan, Y.-S. Hu, L. Chen, Room-temperature stationary sodium-ion batteries for large-scale electric energy storage, Energy Environ. Sci., 6 (2013) 2338-2360.
[4] Y. Lu, L. Wang, J. Cheng, J.B. Goodenough, Prussian blue: a new framework of electrode materials for sodium batteries, Chem. Commun., 48 (2012) 6544-6546.
[5] X. Wu, W. Deng, J. Qian, Y. Cao, X. Ai, H. Yang, Single-crystal FeFe(CN)6 nanoparticles: a high capacity and high rate cathode for Na-ion batteries, J. Mater. Chem. A, 1 (2013) 10130-10134.
[6] Y. You, X.-L. Wu, Y.-X. Yin, Y.-G. Guo, High-quality Prussian blue crystals as superior cathode materials for room-temperature sodium-ion batteries, Energy Environ. Sci., 7 (2014) 1643-1647.
[7] L. Wang, J. Song, R. Qiao, L.A. Wray, M.A. Hossain, Y.-D. Chuang, W. Yang, Y. Lu, D. Evans, J.-J. Lee, S. Vail, X. Zhao, M. Nishijima, S. Kakimoto, J.B. Goodenough, Rhombohedral Prussian White as Cathode for Rechargeable Sodium-Ion Batteries, JACS, 137 (2015) 2548-2554.
[8] T. Matsuda, M. Takachi, Y. Moritomo, A sodium manganese ferrocyanide thin film for Na-ion batteries, Chem. Commun., 49 (2013) 2750-2752.
[9] L. Wang, Y. Lu, J. Liu, M. Xu, J. Cheng, D. Zhang, J.B. Goodenough, A Superior Low-Cost Cathode for a Na-Ion Battery, Angew. Chem. Int. Ed., 52 (2013) 1964-1967.
[10] J. Song, L. Wang, Y. Lu, J. Liu, B. Guo, P. Xiao, J.-J. Lee, X.-Q. Yang, G. Henkelman, J.B. Goodenough, Removal of Interstitial H2O in Hexacyanometallates for a Superior Cathode of a Sodium-Ion Battery, JACS, 137 (2015) 2658-2664.
[11] Y. Moritomo, M. Takachi, Y. Kurihara, T. Matsuda, Synchrotron-Radiation X-Ray Investigation of Li+/Na+ Intercalation into Prussian Blue Analogues, Adv. Mater. Sci. Eng., 2013 (2013) 17.
[12] M. Giorgetti, M. Berrettoni, Structure of Fe/Co/Ni Hexacyanoferrate As Probed by Multiple Edge X-ray Absorption Spectroscopy, Inorg. Chem., 47 (2008) 6001-6008.
[13] M. Giorgetti, L. Guadagnini, D. Tonelli, M. Minicucci, G. Aquilanti, Structural characterization of electrodeposited copper hexacyanoferrate films by using a spectroscopic multi-technique approach, PCCP, 14 (2012) 5527-5537.
[14] M. Giorgetti, A Review on the Structural Studies of Batteries and Host Materials by X-Ray Absorption Spectroscopy, ISRN Materials Science, 2013 (2013) 22.
[15] A.P. Hammersley, S.O. Svensson, M. Hanfland, A.N. Fitch, D. Hausermann, Two-dimensional detector software: From real detector to idealised image or two-theta scan, High Press. Res., 14 (1996) 235-248.
[16] B. Ravel, M. Newville, ATHENA, ARTEMIS, HEPHAESTUS: data analysis for X-ray absorption spectroscopy using IFEFFIT, Journal of Synchrotron Radiation, 12 (2005) 537-541.
[17] C.M. Kareis, S.H. Lapidus, J.-H. Her, P.W. Stephens, J.S. Miller, Non-Prussian Blue Structures and Magnetic Ordering of Na2MnII[MnII(CN)6] and Na2MnII[MnII(CN)6]·2H2O, JACS, 134 (2012) 2246-2254.
[18] G. Małecki, A. Ratuszna, Crystal structure of cyanometallates Me3[Co(CN)6]2 and KMe[Fe(CN)6] with Me=Mn2+, Ni2+, Cu2+, Powder Diffr., 14 (1999) 25-30.
[19] T. Matsuda, J. Kim, Y. Moritomo, Symmetry Switch of Cobalt Ferrocyanide Framework by Alkaline Cation Exchange, JACS, 132 (2010) 12206-12207.

[20] Y. Moritomo, T. Matsuda, Y. Kurihara, J. Kim, Cubic-Rhombohedral Structural Phase Transition in Na1.32Mn[Fe(CN)6]0.83·3.6H2O, J. Phys. Soc. Jpn., 80 (2011) 074608.
[21] D. Buchholz, J. Li, S. Passerini, G. Aquilanti, D. Wang, M. Giorgetti, X-ray Absorption Spectroscopy Investigation of Lithium-Rich, Cobalt-Poor Layered-Oxide Cathode Material with High Capacity, ChemElectroChem, 2 (2015) 85-97.
[22] R. Shannon, Revised effective ionic radii and systematic studies of interatomic distances in halides and chalcogenides, Acta Crystallogr., A, 32 (1976) 751-767.
[23] N. Imanishi, T. Morikawa, J. Kondo, Y. Takeda, O. Yamamoto, N. Kinugasa, T. Yamagishi, Lithium intercalation behavior into iron cyanide complex as positive electrode of lithium secondary battery, J. Power Sources, 79 (1999) 215-219.
[24] M. Ujvari, G. Lang, On the stability of perchlorate ions against reductive attacks in electrochemical systems and in the environment, J. Electrochem. Sci. Eng., 1 (2011) 1-26.
[25] J. Vetter, P. Novák, M.R. Wagner, C. Veit, K.C. Möller, J.O. Besenhard, M. Winter, M. Wohlfahrt-Mehrens, C. Vogler, A. Hammouche, Ageing mechanisms in lithium-ion batteries, J. Power Sources, 147 (2005) 269-281.
[26] M.M. Thackeray, Structural Considerations of Layered and Spinel Lithiated Oxides for Lithium Ion Batteries, J. Electrochem. Soc., 142 (1995) 2558-2563.
[27] S. Watanabe, M. Kinoshita, T. Hosokawa, K. Morigaki, K. Nakura, Capacity fading of LiAlyNi1−x−yCoxO2 cathode for lithium-ion batteries during accelerated calendar and cycle life tests (effect of depth of discharge in charge–discharge cycling on the suppression of the micro-crack generation of LiAlyNi1−x−yCoxO2 particle), J. Power Sources, 260 (2014) 50-56.
[28] Y. Xia, T. Sakai, T. Fujieda, X.Q. Yang, X. Sun, Z.F. Ma, J. McBreen, M. Yoshio, Correlating Capacity Fading and Structural Changes in Li1 + y Mn2 − y O 4 − δ Spinel Cathode Materials: A Systematic Study on the Effects of Li/Mn Ratio and Oxygen Deficiency, J. Electrochem. Soc., 148 (2001) A723-A729.
[29] K. Momma, F. Izumi, VESTA 3 for three-dimensional visualization of crystal, volumetric and morphology data, J. Appl. Crystallogr., 44 (2011) 1272-1276.

Figures

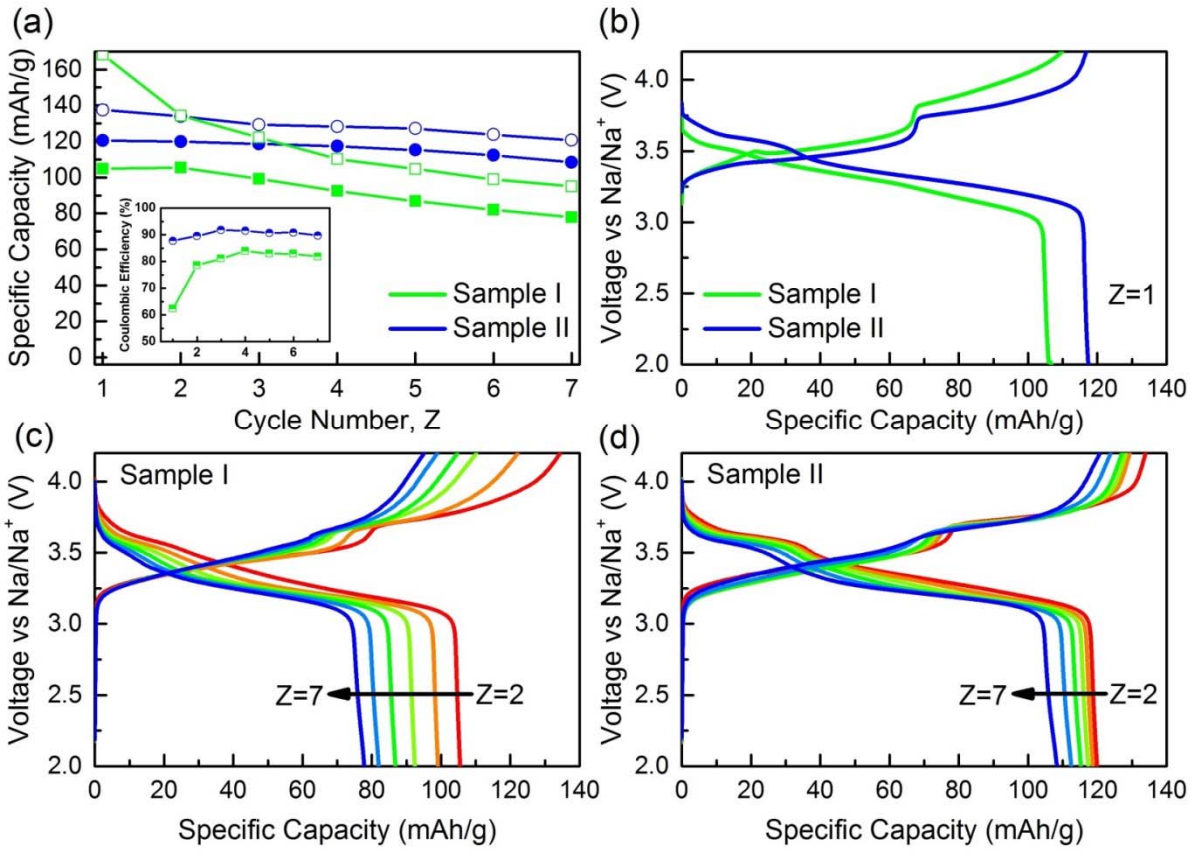

Figure 1. The figure shows (a) specific charge/discharge capacity (empty/filled symbols) and Coulombic efficiency (inset) versus cycle number (Z); (b) first galvanostatic cycle in the synchrotron cell and (c),(d) subsequent cycles for samples **I** and **II** (1C ≡ 120mA/g).

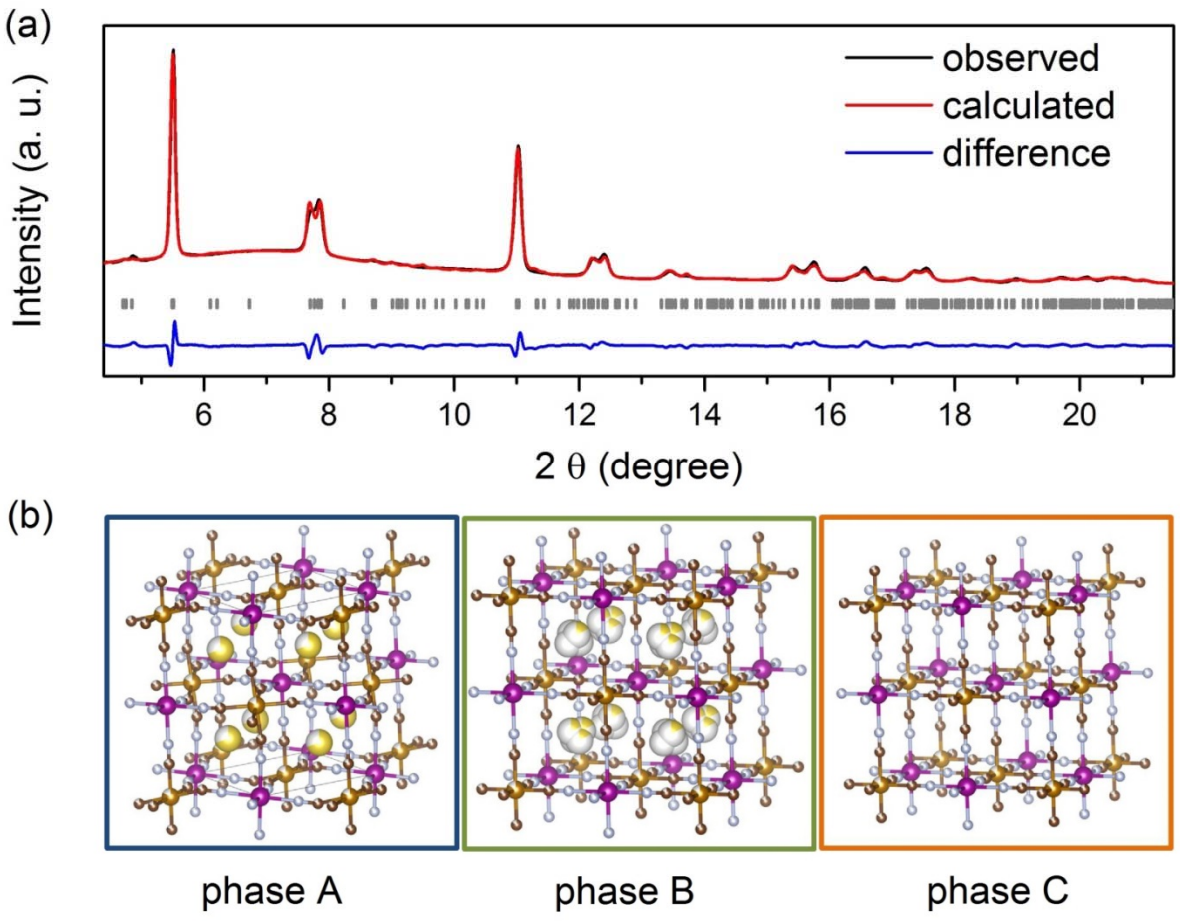

Figure 2 (a) Rietveld refinement of sample **I** (λ = 0.50497 Å) using phase **A**. The background was fitted using a structureless phase with equally spaced broad reflections. (b) Visualization of the different phases by VESTA [29]. Mn, N, C, Fe and Na atoms are represented by purple, gray, brown, light brown and yellow balls, respectively. Partially filled (partially white) balls represent the partial occupancy of certain sites. Water is not represented for clarity.

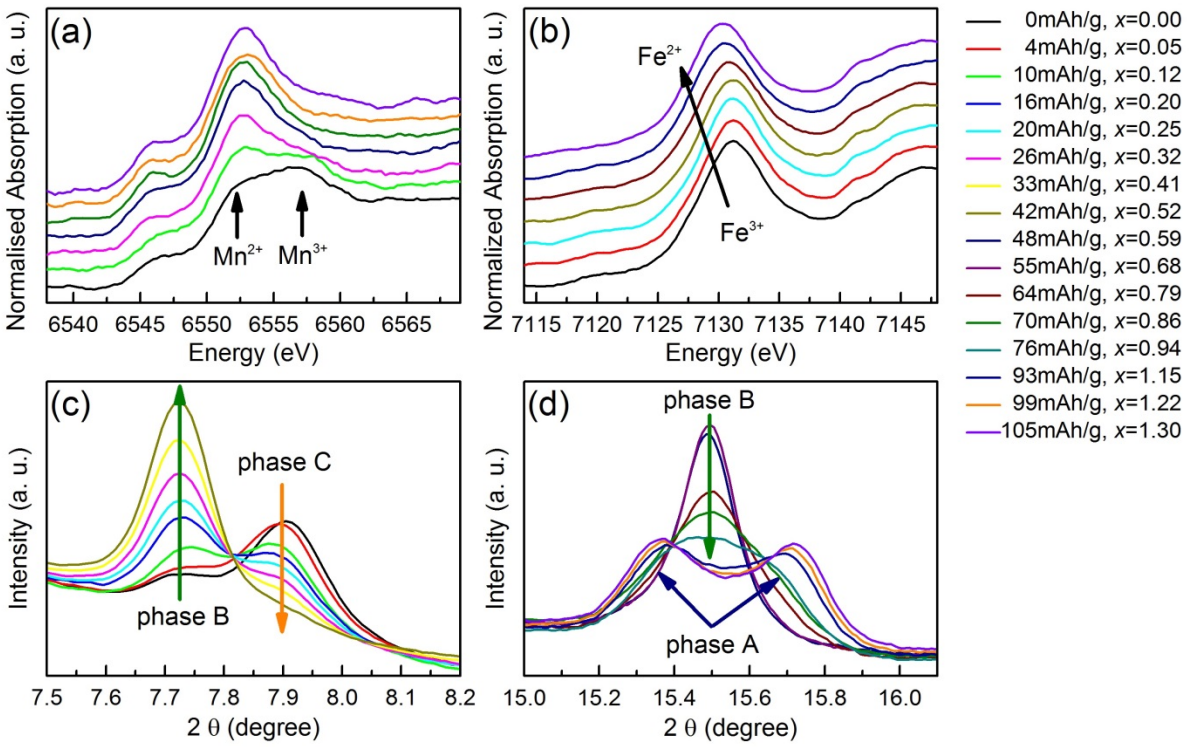

Figure 3 The figure shows changes in normalised XANES spectra and XRD profiles (λ = 0.50497 Å) with increasing capacity / Na content in $Na_xMn[Fe(CN)_6]_{0.83}$ during discharge of sample **I**: Normalised X-ray absorption signal at the Mn (a) and Fe (b) K-edges; (c) Bragg reflections of the cubic (2 2 0) of phase C and **B**; and (d) Bragg reflections of the cubic (4 2 0) of phase **B** which is split in phase **A**. A shift in the absorption edge position of an element to higher (lower) energies corresponds to an increase (decrease) of its average oxidation state. Relative intensities of the reflections correspond approximately to the individual phase fractions.

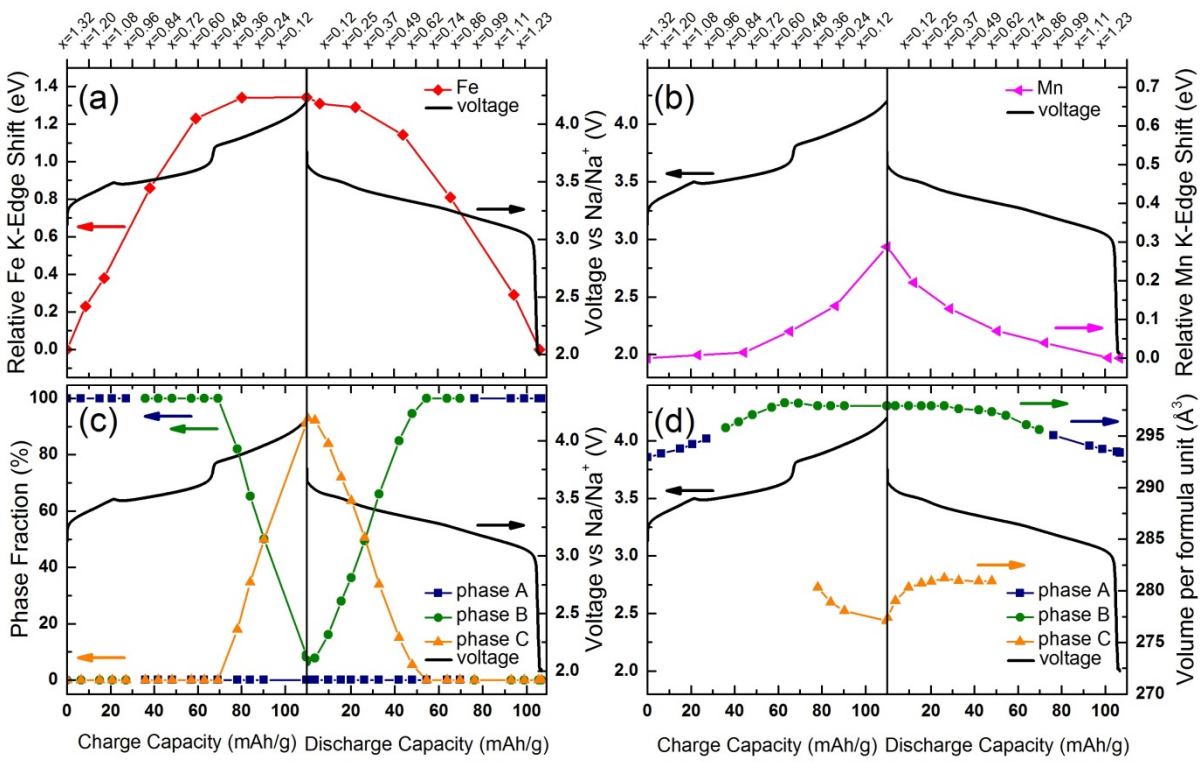

Figure 4 The figure shows the relative shift in absorption edge energy of Fe (a) and Mn (b); the relative phase fractions for the distinct phases **A**, **B** and **C** (c) and the volume per formula unit (d) compared to the voltage profile (black line) as a function of the specific capacity/Na content in $Na_xMn[Fe(CN)_6]_{0.83}$ (bottom/top axis) for sample **I**. R-values are reported in Table S1. Lines are shown as a guide to the eye.

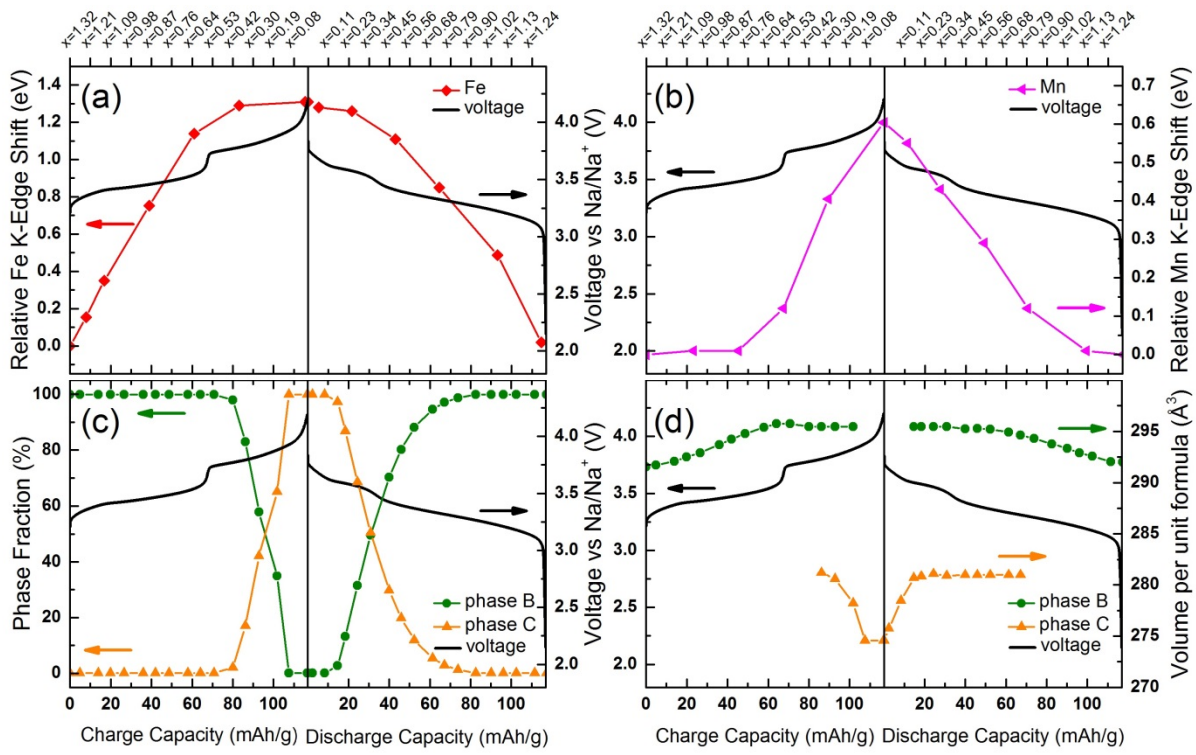

Figure 5 The figure shows the relative shift in absorption edge energy of Fe (a) and Mn (b); the relative phase fractions for the distinct phases **B** and C (c) and the volume per formula unit (d) compared to the voltage profile (black line) as a function of the specific capacity/Na content in $Na_xMn[Fe(CN)_6]_{0.83}$ (bottom/top axis) for sample **II**. R-values are reported in Table S2. Lines are shown as a guide to the eye.

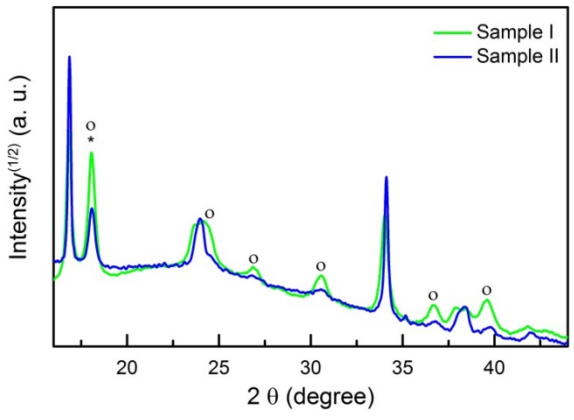

Figure 6 *Ex situ* XRD profiles (Cu Kα1) of samples **I** and **II** cycled for 5 times between 2 V and 4.2 V. The symbols ^{O} and * mark reflections from $NaMnCl_3$ (PDF-number 01-070-1322) and PTFE binder, respectively. The background is dominated by diffuse scattering from the amorphous carbon black in the presented region.

Table 1 Results of the Rietveld refinements of $Na_{1.32}Mn[Fe(CN)_6]_{0.83}\cdot z\ H_2O$.

	sample **I**	sample **II**
z	3.0	2.2
phase	A	B
space group	$P2_1/n$	$Fm\text{-}3m$
Z	2	4
a (Å)	10.543(1)	10.5212(2)
b (Å)	7.457(1)	
c (Å)	7.403(1)	
β **(º)**	91.81(1)	
R_p **(%)**	2.44	0.92
R_{wp} **(%)**	3.42	1.33
R_{exp} **(%)**	21.43	27.26